RESEARCH ARTICLE | APRIL 22 2024

## Fluorite-structured high-entropy oxide sputtered thin films from bixbyite target *⊙*

Special Collection: Era of Entropy: Synthesis, Structure, Properties, and Applications of High-Entropy Materials

George N. Kotsonis ; Saeed S. I. Almishal (); Leixin Miao (); Mary Kathleen Caucci (); Gerald R. Bejger (); Sai Venkata Gayathri Ayyagari (); Tyler W. Valentine (); Billy E. Yang; Susan B. Sinnott (); Christina M. Rost (); Nasim Alem; Jon-Paul Maria



Appl. Phys. Lett. 124, 171901 (2024) https://doi.org/10.1063/5.0201419





#### Articles You May Be Interested In

Achieved limit thermal conductivity and enhancements of mechanical properties in fluorite RE<sub>3</sub>NbO<sub>7</sub> via entropy engineering

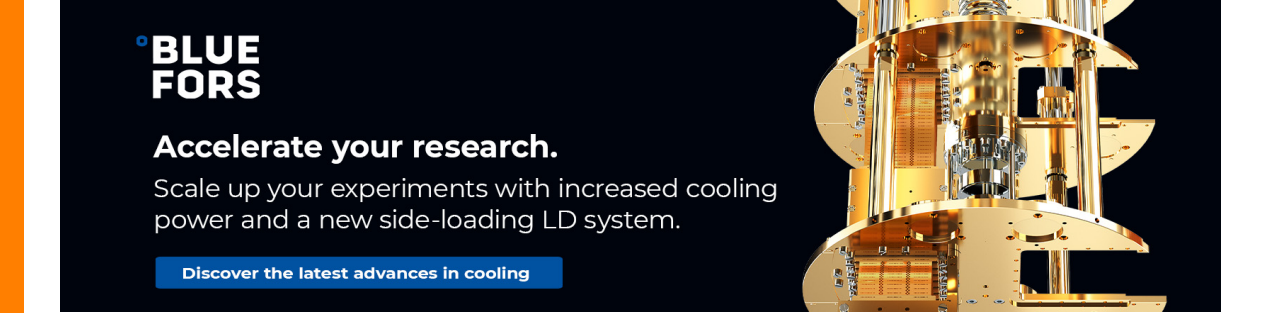
Appl. Phys. Lett. (February 2021)

Large atomic displacements act as dominators for reducing thermal conductivity in  $Y_{3-x}A_xNbO_7$  (A = Ca, In, Mg, Al; x = 0.05, 0.1) fluorites

Appl. Phys. Lett. (October 2024)

Correlation between anion related defects and ion beam induced luminescence in Y<sub>4</sub>Zr<sub>3</sub>O<sub>12</sub>

Appl. Phys. Lett. (July 2021)





# Fluorite-structured high-entropy oxide sputtered thin films from bixbyite target

Cite as: Appl. Phys. Lett. **124**, 171901 (2024); doi: 10.1063/5.0201419 Submitted: 30 January 2024 · Accepted: 4 April 2024 · Published Online: 22 April 2024







George N. Kotsonis, Daeed S. I. Almishal, Delixin Miao, Delixin Miao, Delixin Mary Kathleen Caucci, Delixin Gerald R. Bejger, Delixin Sai Venkata Gayathri Ayyagari, Delixin Tyler W. Valentine, Delixin Billy E. Yang, Susan B. Sinnott, Delixin Delixina M. Rost, Delixin Alem, and Jon-Paul Maria

#### **AFFILIATIONS**

**Note:** This paper is part of the APL Special Collection on Era of Entropy: Synthesis, Structure, Properties, and Applications of High Entropy Materials.

a) Author to whom correspondence should be addressed: saeedsialmishal@gmail.com

#### **ABSTRACT**

The prototype high-entropy oxide (HEO)  $Y_{0.2}La_{0.2}Ce_{0.2}Pr_{0.2}Sm_{0.2}O_{2-\delta}$  represents a particularly complex class of HEOs with significant anion sublattice entropy. The system takes either a fluorite or bixbyite-type crystal structure, depending on synthesis kinetics and thermal history. Here, we synthesize bulk ceramics and epitaxial thin films of  $Y_{0.2}La_{0.2}Ce_{0.2}Pr_{0.2}Sm_{0.2}O_{2-\delta}$  and use diffraction to explore crystal symmetry and phase. Thin films exhibit the high symmetry fluorite phase, while bulk ceramics adopt the lower symmetry bixbyite phase. The difference in chemical ordering and observed symmetry between vapor-deposited and reactively sintered specimens suggests that synthesis kinetics can influence accessible local atomic configurations, i.e., the high kinetic energy adatoms quench in a higher-effective temperature, and thus higher symmetry structure with more configurational entropy. More generally, this demonstration shows that recovered HEO specimens can exhibit appreciably different local configurations depending on synthesis kinetics, with potential ramifications on macroscopic physical properties.

Published under an exclusive license by AIP Publishing. https://doi.org/10.1063/5.0201419

High-entropy oxides (HEOs) are complex oxide solid solutions, typically composed of four or more parent oxide endmembers in roughly equal proportions. In 2015, Rost *et al.* demonstrated entropy stabilization in the  $Mg_{0.2}Co_{0.2}Ni_{0.2}Cu_{0.2}Zn_{0.2}O$  system, which equilibrates as a rock salt solid solution above ~875 °C. The community has since synthesized HEOs with many other binary and ternary crystal structures. Among them, defective fluorite-structured HEOs are of great interest as they can span a wide range of net valence states and oxygen vacancy concentration depending on their cation formulation. Yo\_2La\_{0.2}Ce\_{0.2}Pr\_{0.2}Sm\_{0.2}O\_{2-\delta} represents a particularly complex and intriguing HEO system, owing to the multivalency of Ce and Pr, as well as the large nominal  $\delta$  value of 0.33. While all HEOs are in part defined by cation disorder,  $Y_{0.2}La_{0.2}Ce_{0.2}Pr_{0.2}Sm_{0.2}O_{2-\delta}$  also exhibits significant anion sublattice disorder. Crystal symmetry and physical and electrochemical properties appear sensitive to both

oxygen stoichiometry and thermal history.  $^{1.3,6}$  Additionally, the intermediate and tunable stoichiometry that can be achieved in  $MO_2$  fluorite and  $M_2O_3$  bixbyite mixtures results in a variable degree of chemical ordering and periodic lattice distortions that determine the macroscopically observed symmetry. In terms of application, defective fluorites such as  $3^+$ -substituted  $CeO_2$  (Ref. 7) are useful oxygen ion conductors. However, conductivity is inhibited at large  $3^+$  cations concentrations by local chemical ordering of oxygen vacancies.  $^{7,8}$  Understanding chemical ordering tendencies as a function of synthesis procedures and identifying paths to stabilize the fluorite structure is a prudent first step toward optimizing the functional properties of fluorite HEOs.

HEO synthesis techniques vary widely in terms of initial state, kinetics, and final microstructure. Dense ceramics can be reactively sintered, powders can be precipitated from a nitrate solution, 3,6,10

<sup>&</sup>lt;sup>1</sup>Department of Materials Science and Engineering, The Pennsylvania State University, University Park, Pennsylvania 16802, USA

<sup>&</sup>lt;sup>2</sup>Department of Chemistry, The Pennsylvania State University, University Park, Pennsylvania 16802, USA

<sup>&</sup>lt;sup>3</sup>Department of Materials Science and Engineering, Virginia Polytechnic Institute and State University, Blacksburg, Virginia 24060, USA

Department of Physics and Astronomy, James Madison University, Harrisonburg, Virginia 22807, USA

<sup>&</sup>lt;sup>5</sup>Institute for Computational and Data Science, The Pennsylvania State University, University Park, Pennsylvania, 16802, USA

and thin films can be grown by physical vapor deposition (PVD). Since HEOs are frequently kinetically quenched for study or application, the initial precursor state and the synthesis kinetics can strongly influence the atomic configuration of the observed final state. Precipitation and PVD enable a short kinetic pathway for nucleation of fully disordered solution configurations. In contrast, solid-state reaction requires longer pathways through configuration space and predispose the system to thermodynamically prescribed atomic configurations closer to equilibrium. For  $Y_{0.2}La_{0.2}Ce_{0.2}Pr_{0.2}Sm_{0.2}O_{2-\delta}$  specifically, solution precipitation and PVD enable nucleation of a metastable disordered fluorite phase, 3.6.16 while reactive sintering limits the system to chemically ordered configurations reminiscent of a bixbyite-type structure.

After initial solution precipitation of fluorite-structured La<sub>0.2</sub>Ce<sub>0.2</sub>Pr<sub>0.2</sub>Sm<sub>0.2</sub>Y<sub>0.2</sub>O<sub>2- $\delta$ </sub> powders, subsequent annealing<sup>3</sup> or reducing<sup>6</sup> procedures produce additional diffraction peaks indicative of symmetry reduction to the bixbyite-type structure observed in reactively sintered specimens. Regarding the lower symmetry bixbyite-type structure, Djenadic *et al.* performed several refinements on powder x-ray diffraction (XRD) data to test various symmetries including  $Ia\bar{3}$ ,  $F\bar{4}3m$ , and  $I2_13.^3$  They settled on a structure with  $Ia\bar{3}$  space group symmetry (typical of Y<sub>2</sub>O<sub>3</sub>), but note that  $F\bar{4}3m$  symmetry more accurately reproduced the low-intensity secondary peaks that differentiate the structure from  $Fm\bar{3}m$  fluorite symmetry.

To clarify some of the structural uncertainty regarding Y<sub>0.2</sub>La<sub>0.2</sub>  $Ce_{0.2}Pr_{0.2}Sm_{0.2}O_{2-\delta}$ , we set out to isolate  $Y_{0.2}La_{0.2}Ce_{0.2}Pr_{0.2}Sm_{0.2}O_{2-\delta}$ crystals with both ordered and disordered oxygen sublattices and characterize them using electron diffraction. To achieve this, we leveraged the starkly contrasting kinetics of two different synthesis methods: magnetron sputtering and reactive sintering. We employ XRD to probe the structure on a macroscopic scale; transmission electron microscopy (TEM) and selected area electron diffraction (SAED) to probe the symmetry on sub-crystal length scales, energy-dispersive spectroscopy (EDS) to probe chemistry and homogeneity on local scale, and x-ray absorption near edge structure (XANES) to probe the local electronic environment with chemical selectivity. We also calculate the enthalpy of formation for the equimolar composition with different crystal symmetries using density functional theory (DFT). Reactively sintered ceramics exhibit a bixbyite-type structure, but with slightly different symmetry than the previously reported Ia3 space group, while thin films exhibit fluorite symmetry. Results are discussed in the context of local symmetry, synthesis kinetics, and pathways through configuration space.

Figures 1(a) and 1(b) present XRD and SEM data for bulk  $Y_{0.2}La_{0.2}Ce_{0.2}Pr_{0.2}Sm_{0.2}O_{2-\delta}$  reactively sintered at 1600 °C for 8 h. The low-intensity superstructure peaks (e.g., 112, 114, 233, and 134) indicate a structure similar to bixbyite, characterized by a measurable amount of local chemical ordering and corresponding periodic lattice distortions. Figure 1(b) reveals a dense microstructure with some grains exceeding 10  $\mu$ m in size. The bulk sample EDS shows homogeneous distribution of cations (supplementary material, Fig. S1). The bixbyite-type diffraction pattern in Fig. 1(a) implies that either 1600 °C provides insufficient energy to allow the formation of fully disordered fluorite configurations, or that our initial 15°/min cooling rate is insufficient to kinetically quench fluorite configurations if they were ever present. Based on the behavior of endmember oxides, we think the former case is more likely, for instance, cubic Sm<sub>2</sub>O<sub>3</sub> does not take a disordered cubic phase with

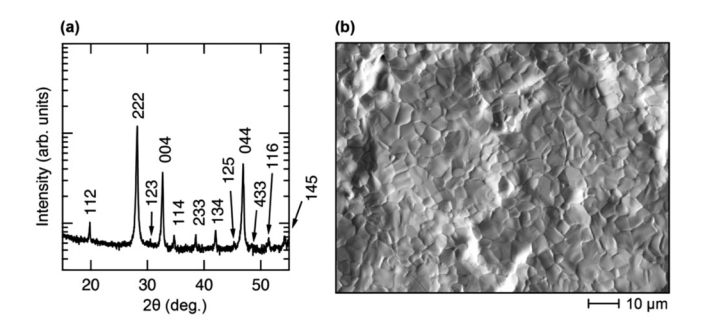


**FIG. 1.** Structural data for reactively sintered  $Y_{0.2}\text{La}_{0.2}\text{Ce}_{0.2}\text{Pr}_{0.2}\text{Sm}_{0.2}\text{O}_{2-\delta}$ : (a) XRD pattern indexed using bixbyite indices and (b) SEM micrograph (a faint hairline fracture can be seen in the lower left of the image, likely induced by differential thermal strain during cooling).

 $Im\bar{3}m$  symmetry until around 2200 °C. <sup>17</sup> Complete long-range order is likely prohibited in  $Y_{0.2}La_{0.2}Ce_{0.2}Pr_{0.2}Sm_{0.2}O_{2-\delta}$  by the intermediate stoichiometry (i.e.,  $\delta \neq 0$ ), so we posit that the local structure is similar to  $CeO_2$ - $Y_2O_3$  solid solutions, which exhibit single-phase diffraction patterns, but localized bixbyite-type ordering and symmetry on subgrain length scales. <sup>18</sup>

The sputtered  $Y_{0.2}La_{0.2}Ce_{0.2}Pr_{0.2}Sm_{0.2}O_{2-\delta}$  thin film XRD and AFM data are depicted in Fig. 2. Figure 2(a) presents XRD data for two 20 nm thick sputtered thin films from the aforementioned bulk sintered target on YSZ substrate at two growth temperatures (300 and 400 °C). Both films appear single-phase and epitaxial, showing only the 00l family of reflections in the XRD pattern. Film grown at 300 °C substrate temperature has a slightly narrower and sharper XRD peak compared to the film grown at 400 °C. Figure 2(b) presents a narrower and higher resolution  $\theta$ -2 $\theta$  pattern for two films grown at 300 °C: 20 nm thick film and a 96 nm thick film. Figure 2(c) presents corresponding rocking curves ( $\omega$  scans at constant  $2\theta$ ) consisting of a superposition of two components, one with a full-width-at-halfmaxima (FWHM) of 0.04° and the other with a FWHM of 1.6°. The narrow component of the rocking curve disappears at higher thicknesses, suggesting structural relaxation as a function of thickness; this is expected due to the appreciable lattice mismatch between the film and substrate (-6.9%). Atomic-resolution STEM imaging in Fig. 2(e) suggests some disorder at the interface and confirms epitaxy with the following in-plane orientational relationship to the YSZ substrate: [100]-Y $_{0.2}$ La $_{0.2}$ Ce $_{0.2}$ Pr $_{0.2}$ Sm $_{0.2}$ O $_{2-\delta}$  || [100]-YSZ. Thickness fringes in Fig. 2(b) and AFM data in Fig. 2(d) suggest a smooth top surface and macroscopically flat film-substrate interface. Overall, the sputtered film exhibits high fidelity, but the data so far does not reveal whether the film exhibits significant chemical ordering. For symmetry characterization and comparison to bulk, we turn to selected area electron diffraction, a proven method for identifying chemical ordering in rare earth oxides with fluorite-related structures.2

The SAED patterns for bulk and sputtered  $Y_{0.2}La_{0.2}Ce_{0.2}Pr_{0.2}Sm_{0.2}O_{2-\delta}$  are shown in Figs. 3(a) and 3(b), respectively. Figures 3(c)-3(e) present simulated SAED patterns from crystal models with  $I2_13$ ,  $Ia\bar{3}$ , and  $Fm\bar{3}m$ , symmetries.  $^{3,21,22}$  Comparison of Figs. 3(b) and 3(e) suggests that the sputtered film exhibits fluorite  $Fm\bar{3}m$  symmetry. The SAED pattern from the bulk specimen in Fig. 3(a) exhibits additional diffraction spots that clearly indicate a lower symmetry than sputtered  $Y_{0.2}La_{0.2}Ce_{0.2}Pr_{0.2}Sm_{0.2}O_{2-\delta}$  in Fig. 3(b).

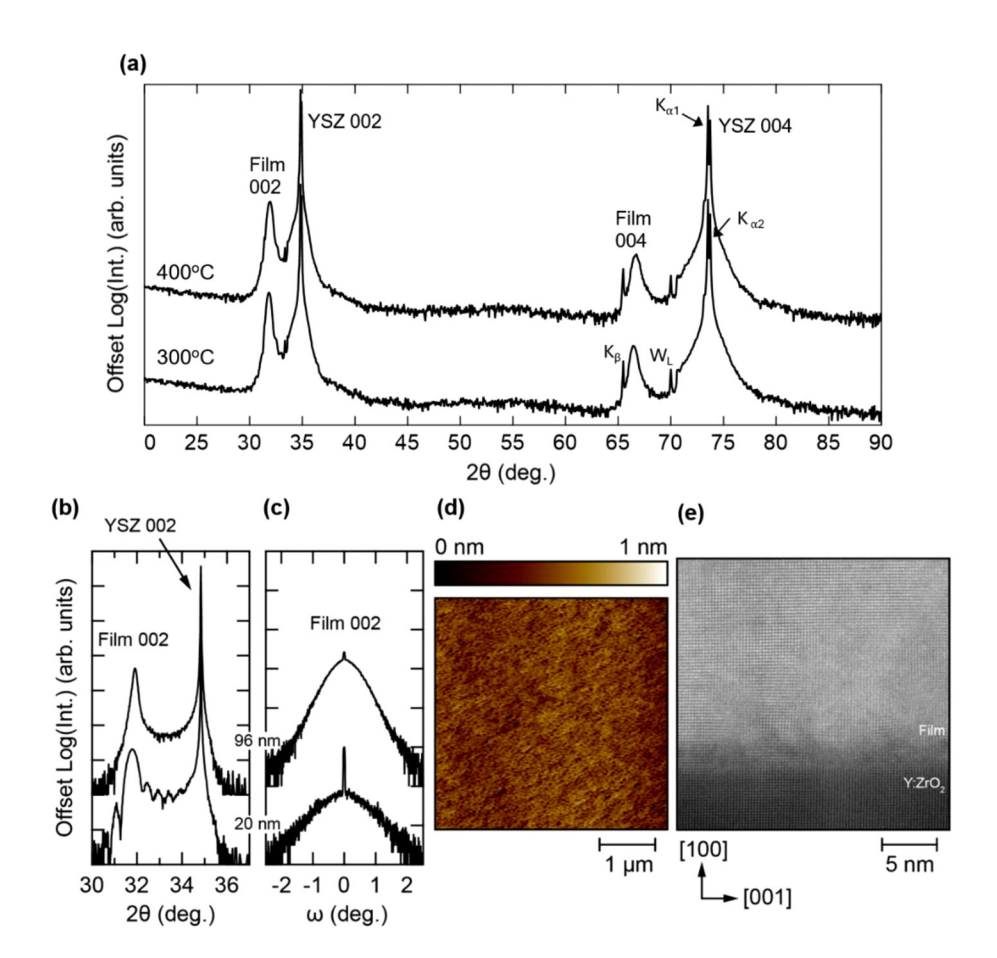


**FIG. 2.** Structural data for sputtered  $\rm Y_{0.2}La_{0.2}$   $\rm Ce_{0.2}Pr_{0.2}Sm_{0.2}O_{2-.5}$ : (a) XRD pattern of two films grown on YSZ at different substrate temperatures; (b) out-of-plane XRD patterns of two films grown on YSZ at 300 °C (thicknesses of 20 or 96 nm), indexed using fluorite indices; (c) corresponding rocking curves; (d) AFM micrograph of the 20 nm film; and (e) HAADF micrograph viewed along the [010] zone axis of the 20 nm film. Film-substrate interface is visible near the bottom of (d).

Focusing on the white-encircled diffraction spots corresponding to {110}, {220}, and {330} lattice planes, we can see that the pattern in Fig. 3(a) exhibits 110 and 330 spots and no visible 220 spot, while the simulated Ia3 pattern exhibits 220 spots and no 110 or 330 diffraction spots (Fig. 3). With  $Ia\bar{3}$  symmetry, {110} and {330} reflections are extinguished by the glide plane symmetry element,<sup>23</sup> which is evidently not present across significant length scales in our bulk sample. Therefore, when indexing the SAED pattern from bulk and comparing it to electron diffraction simulations with  $I2_13$ ,  $Ia\bar{3}$ , and  $Fm\bar{3}m$  symmetries, we find that  $I2_13$  simulated pattern is the best match to our experimental pattern, which exhibits 110 and 330 spots, but only faint 220 spots. We observe that the enthalpy of formation  $\Delta H_f$  predicted from DFT exhibit roughly similar values for both I213 and Ia3 symmetries (see Table I) with both being lower than the "metastabilized"  $Fm\bar{3}m$  symmetry. This corroborates the difficulties in discerning the bulk system symmetry. It is also likely that the true symmetry of bulk  $Y_{0.2}La_{0.2}Ce_{0.2}Pr_{0.2}Sm_{0.2}O_{2-\delta}$  samples fluctuates spatially (e.g., as in CeO<sub>2</sub>-Y<sub>2</sub>O<sub>3</sub> solid solutions, which can exhibit localized chemical ordering<sup>18</sup>) and complete determination likely requires diffraction along different zone axes with more rigorous analysis. We believe the present result provides a step toward unraveling the structural tendencies of  $Y_{0.2}La_{0.2}Ce_{0.2}Pr_{0.2}Sm_{0.2}O_{2-\delta}$  and similar systems, given that bulk and powder XRD patterns can be inconclusive or misleading as the subtle changes produced by anion sublattice disorder can be difficult to differentiate.

Figure 4 presents XANES data collected for both sputtered and bulk  $Y_{0.2}La_{0.2}Ce_{0.2}Pr_{0.2}Sm_{0.2}O_{2-\delta}$ . The XANES spectra of the La and Sm L<sub>3</sub>-edges are monotonous, which complicates the qualitive analysis.<sup>24,25</sup> However, data from the Y K-edge, Ce L<sub>3</sub>-edge, and the Pr L<sub>3</sub>edge is very informative. The Y K-edge of Y2O3 consists of a doublet with peaks at  $\sim$ 17 053 and  $\sim$ 17 063 eV. The latter peak is likely due to the presence of Y in a six coordinated environment, which decreases in intensity with coordination number.<sup>26</sup> This is seen in the (Y, Co) doped CeO2 reference where Y has an eight coordinated environment. Thus, the flattening of the sputtered and bulk  $Y_{0.2}La_{0.2}Ce_{0.2}Pr_{0.2}Sm_{0.2}O_{2-\delta}$  Y K-edge doublet is indicative of a mixed coordination environment. The Ce L<sub>3</sub>-edge of CeO<sub>2</sub> has three notable features, a Ce3+ shoulder on the white line at  $\sim$ 5725 eV, and a peak doublet with peaks at  $\sim$ 5733 and  $\sim$ 5743 eV. <sup>28,29</sup> The first peak in the doublet is associated with 4f occupancy in the final state, while the second peak is due to absorption into the 5d level with no occupancy in the 4f level, which is a Ce4+ signature.<sup>29</sup> Our measured spectra for the Ce  $L_3$ -edges are comparable to the  $CeO_2$  standard, indicating a mixed valence state with a majority of Ce being 4+. There is a slight difference, however, in the intensity of the latter peak in the doublet of the measured samples, which we attribute to the local disorder around the Ce cations in our samples. Pr<sub>6</sub>O<sub>11</sub> Pr L<sub>3</sub>-edge is similar to that of  $CeO_2$ , where there exists a shoulder on the white line at  $\sim$ 5970 eV associated with Pr 3+, and a peak doublet at ~5975 and ~5985 eV associated with Pr 3+. Although the majority of Pr is 4+ in our

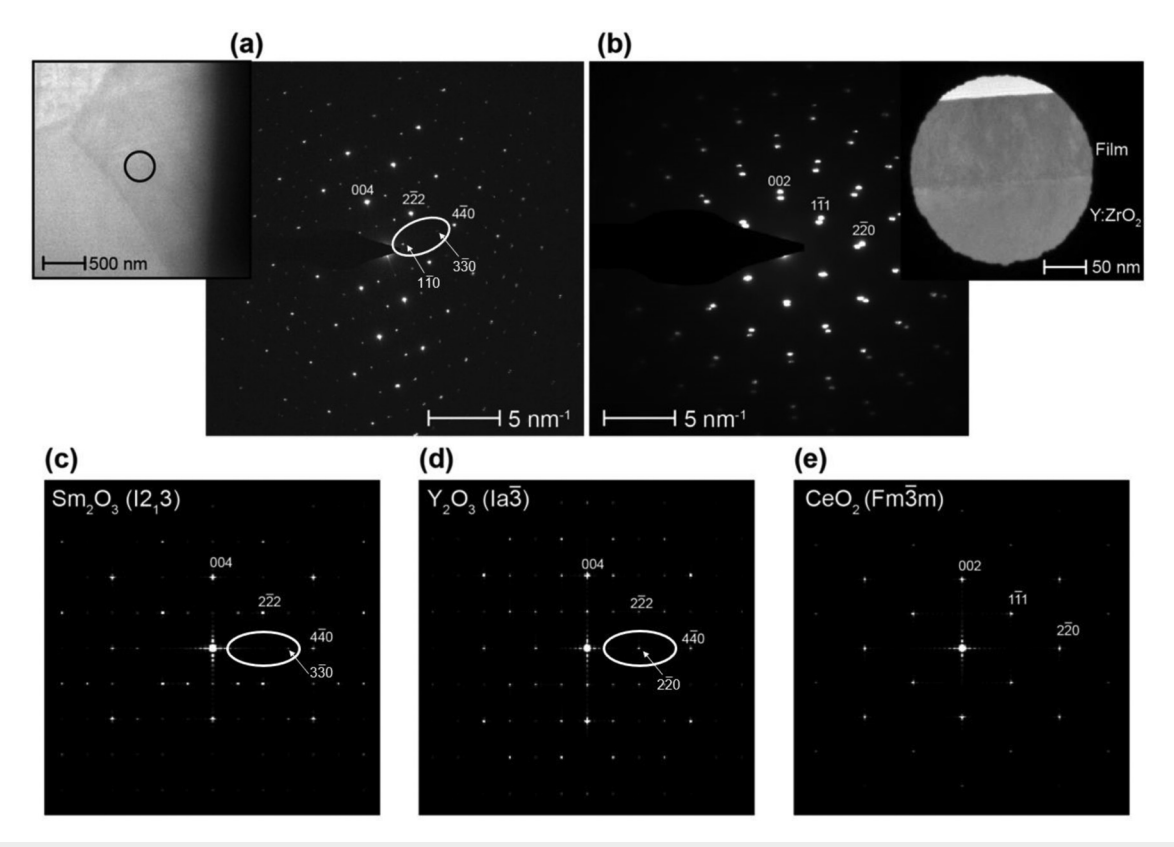


FIG. 3. SAED micrographs of bulk and sputtered  $Y_{0.2}La_{0.2}Ce_{0.2}Pr_{0.2}Sm_{0.2}O_{2-\delta}$  viewed along the [1  $\bar{1}$  0] zone axis and simulated SAED patterns for comparison: (a) bulk  $Y_{0.2}La_{0.2}Ce_{0.2}Pr_{0.2}Sm_{0.2}O_{2-\delta}$ ; (b) sputtered  $Y_{0.2}La_{0.2}Ce_{0.2}Pr_{0.2}Sm_{0.2}O_{2-\delta}$ ; and (c)–(e) SAED patterns simulated from crystal models with  $I2_13$ ,  $Ia\bar{3}$ , and  $Fm\bar{3}m$  symmetries, respectively. Pattern in (a) partially indexed using bixbyite indices and pattern in (b) partially indexed using fluorite indices. Insets in (a) and (b) show traditional TEM micrographs with the isolated region used to collect SAED data in (a) denoted by a black circle. Signal from both the film and substrate can be seen in (b).

**TABLE I.** The high-entropy composition calculated enthalpy of formation  $\Delta H_{f}$ .

Supercell model formula	Formula	Space group	$\Delta H_f$ (eV/atom)	
Ce <sub>7</sub> La <sub>6</sub> Pr <sub>7</sub> Sm <sub>6</sub> Y <sub>6</sub> O <sub>54</sub> Ce <sub>7</sub> La <sub>6</sub> Pr <sub>7</sub> Sm <sub>6</sub> Y <sub>6</sub> O <sub>54</sub> Ce <sub>7</sub> La <sub>6</sub> Pr <sub>7</sub> Sm <sub>6</sub> Y <sub>6</sub> O <sub>54</sub>	$\begin{split} &Y_{0.2} La_{0.2} Ce_{0.2} Pr_{0.2} Sm_{0.2} O_{2-\delta} \ (\delta=0.3125) \\ &Y_{0.4} La_{0.4} Ce_{0.4} Pr_{0.4} Sm_{0.4} O_{3+\delta} \ (\delta=0.375) \\ &Y_{0.4} La_{0.4} Ce_{0.4} Pr_{0.4} Sm_{0.4} O_{3+\delta} \ (\delta=0.375) \end{split}$	Fm3̄ m Ia3̄ I2₁3	-3.407 -3.449 -3.444	

measured bulk sample, the shift to lower energy in the Pr  $L_3$ -edge peaks suggests a higher fraction of 3+ than the  $Pr_6O_{11}$  standard. These observations demonstrate the possible spectrum of local cation environments in  $Y_{0.2}La_{0.2}Ce_{0.2}Pr_{0.2}Sm_{0.2}O_{2-\delta}$ , the similarities of their spectral signatures, and the difficulty to accurately assign structures in these complex crystals, and thus draw conclusions regarding entropic effects.

Collectively, the specimens reactively sintered at 1500 °C exhibit a lower symmetry diffraction pattern indicative of the chemically ordered bixbyite-type, while the highly non-equilibrium synthesis kinetics result in crystalline films with fluorite symmetry in  $Y_{0.2}La_{0.2}Ce_{0.2}Pr_{0.2}Sm_{0.2}O_{2-\delta}$ . Symmetry reduction from fluorite structure to the bixbyite-type structure upon annealing or exposure to a reducing gas indicates a relative thermodynamic stability of ordered

anion configurations compared to disordered ones. So Given the endmember chemical ordering tendencies, which are largest at low temperatures,  $^{17,20}$  one may anticipate the lower symmetry structure to emerge at lower synthesis temperatures, somewhat analogous to the Bi<sub>2</sub>O<sub>3</sub> system, in which the disordered cubic fluorite  $\delta$ -phase is only stable above 750 °C. So On the contrary, reports for powder precipitation at 750 and 1150 °C. and our film growth at 600 °C and lower produce the high temperature structure metastabilized at room temperature. These observations necessitate a kinetic, rather than thermodynamic, explanation. In PVD and chemical precipitation processes, sputter vapor production and chemical dissolution induces a precursor initial state where mixing is completely random and uniform, from which crystallization will occur. In this case, the crystal that will form with the smallest diffusion budget is one with a similarly random and

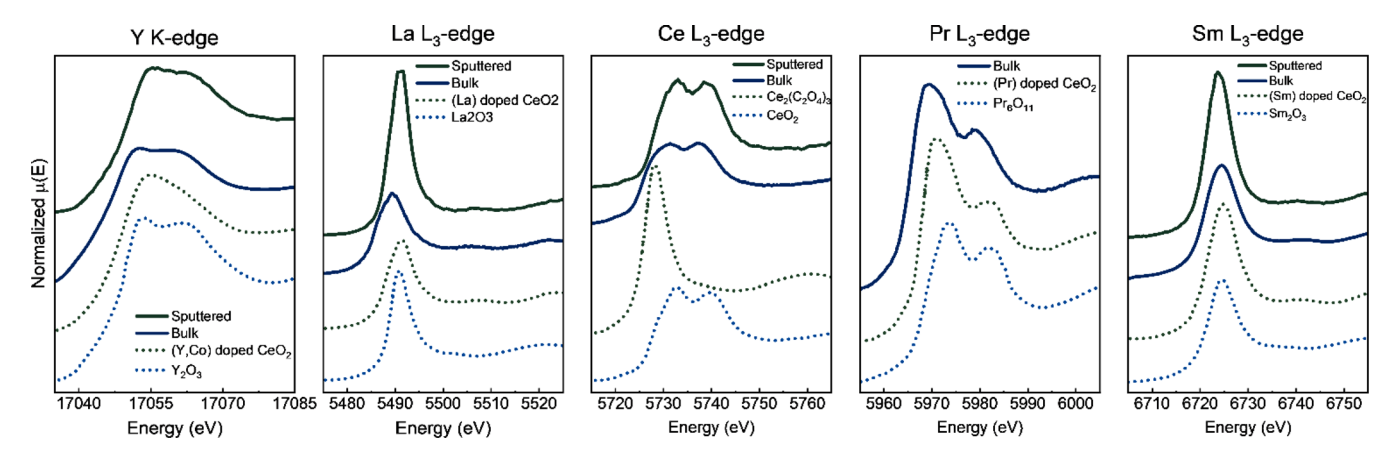


FIG. 4. XANES data for bulk and sputtered  $Y_{0.2}La_{0.2}Ce_{0.2}Pr_{0.2}Sm_{0.2}O_{2-\delta}$ : for Ce, La, Sm, and Y absorbers, respectively, along with reference patterns. Pr XANES is only available for the bulk sample at the time of measurement.

uniform cation distribution. Furthermore, in the case of PVD, the substantial adatom kinetic energy induces a high effective temperature that, during landing, will promote a high-entropy and high-symmetry state. Finally, especially in refractory systems like this, with modest substrate temperatures, this high-entropy state is likely to be preserved metastably. On the other hand, during solid state reaction, the system begins in a very low entropy initial state where chemical entities are physically segregated at the micrometer scale (i.e., individual powder particles). Entropy must increase during synthesis, and the system as a whole is configurationally limited to thermodynamically prescribed assemblies, which appear to exhibit enough chemical ordering to produce low symmetry non-fluorite diffraction patterns in  $Y_{0.2}La_{0.2}Ce_{0.2}Pr_{0.2}Sm_{0.2}O_{2-\delta}$  specimens.

While the present study is limited to  $Y_{0.2}La_{0.2}Ce_{0.2}Pr_{0.2}Sm_{0.2}O_{2-\delta}$ , we believe other systems with significant anion disorder, chemical ordering tendencies, or metastability in general may exhibit similar kinetic behavior. Furthermore, the chemical flexibility of HEOs might allow tunable symmetry and local chemical ordering tendencies depending on cation selection and susceptibility to reduction or oxidation. In other words, cation selection and stoichiometric control should provide a means to alter the balance between the high entropy associated with a disordered anion sublattice and the relatively low enthalpy associated with an ordered one. Composition and net valence control, combined with the kinetic dependence shown here, should facilitate a wide variety of fluorite-derived HEO systems with tunable symmetry and physical properties.

In the broader context of HEOs, the observation presented here suggest that non-equilibrium processing techniques can enable recovery of configurations corresponding to higher-entropy macrostates compared to near-equilibrium processing techniques. These observations, combined with the compositional flexibility inherent to HEO systems, should facilitate further investigations into the wealth of possible fluorite-derived HEOs.

See the supplementary material for a detailed description of the experimental and computational methods. It also includes EDS maps for bulk  $Y_{0.2}La_{0.2}Ce_{0.2}Pr_{0.2}Sm_{0.2}O_{2-\delta}$ .

The authors acknowledge the use of facilities and instrumentation supported by NSF through the Pennsylvania State University Materials Research Science and Engineering Center (No. DMR-2011839).

### AUTHOR DECLARATIONS Conflict of Interest

The authors have no conflicts to disclose.

#### **Author Contributions**

George N. Kotsonis: Conceptualization (lead); Data curation (equal); Formal analysis (lead); Methodology (equal); Validation (equal); Visualization (equal); Writing - original draft (lead). Saeed S. I. Almishal: Conceptualization (supporting); Data curation (supporting); Formal analysis (equal); Investigation (supporting); Methodology (equal); Validation (lead); Visualization (lead); Writing - review & editing (lead). Leixin Miao: Conceptualization (equal); Data curation (lead); Formal analysis (equal); Methodology (equal); Validation (equal); Visualization (equal); Writing - original draft (equal). Mary Kathleen Caucci: Data curation (supporting); Formal analysis (supporting); Investigation (equal); Methodology (equal); Validation (supporting); Writing - review & editing (supporting). Gerald R. Bejger: Formal analysis (supporting); Validation (supporting); Visualization (supporting); Writing - review & editing (supporting). Sai Venkata Gayathri Ayyagari: Data curation (supporting); Formal analysis (supporting); Validation (supporting); Writing - original draft (supporting); Writing - review & editing (supporting). Tyler W. Valentine: Data curation (equal); Formal analysis (equal); Validation (supporting); Visualization (supporting); Writing – original draft (supporting). Billy E. Yang: Validation (supporting); Writing - review & editing (supporting). Susan B. Sinnott: Methodology (equal); Resources (equal); Supervision (equal); Validation (equal). Christina M. Rost: Conceptualization (equal); Formal analysis (equal); Methodology (equal); Resources (equal); Supervision (equal); Validation (equal); Writing - review & editing (equal). Nasim Alem: Methodology (equal); Resources (equal); Supervision (equal); Validation (equal). Jon-Paul Maria: Conceptualization (equal); Formal analysis (equal);

Methodology (equal); Resources (equal); Supervision (equal); Validation (equal); Writing – review & editing (equal).

#### **DATA AVAILABILITY**

The data that support the findings of this study are available from the corresponding author upon reasonable request.

#### **REFERENCES**

- <sup>1</sup>G. N. Kotsonis, S. S. I. Almishal, F. Marques dos Santos Vieira, V. H. Crespi, I. Dabo, C. M. Rost, and J.-P. Maria, "High-entropy oxides: Harnessing crystalline disorder for emergent functionality," J. Am. Ceram. Soc. 106, 5587–5611 (2023)
- <sup>2</sup>C. M. Rost, E. Sachet, T. Borman, A. Moballegh, E. C. Dickey, D. Hou, J. L. Jones, S. Curtarolo, and J.-P. Maria, "Entropy-stabilized oxides," Nat. Commun. 6, 8485 (2015).
- <sup>3</sup>R. Djenadic, A. Sarkar, O. Clemens, C. Loho, M. Botros, V. S. K. Chakravadhanula, C. Kübel, S. S. Bhattacharya, A. S. Gandhi, and H. Hahn, "Multicomponent equiatomic rare earth oxides," Mater. Res. Lett. 5, 102–109 (2017).
- <sup>4</sup>j. Gild, M. Samiee, J. L. Braun, T. Harrington, H. Vega, P. E. Hopkins, K. Vecchio, and J. Luo, "High-entropy fluorite oxides," J. Eur. Ceram. Soc. 38, 3578–3584 (2018).
- 5K. Chen, X. Pei, L. Tang, H. Cheng, Z. Li, C. Li, X. Zhang, and L. An, "A five-component entropy-stabilized fluorite oxide," J. Eur. Ceram. Soc. 38, 4161–4164 (2018).
- <sup>6</sup>A. Sarkar, B. Eggert, L. Velasco, X. Mu, J. Lill, K. Ollefs, S. S. Bhattacharya, H. Wende, R. Kruk, R. A. Brand, and H. Hahn, "Role of intermediate 4f states in tuning the band structure of high entropy oxides," APL Mater. 8, 051111 (2020).
- <sup>7</sup>S. Omar, E. D. Wachsman, J. L. Jones, and J. C. Nino, "Crystal structure-ionic conductivity relationships in doped ceria systems," J. Am. Ceram. Soc. **92**, 2674–2681 (2009).
- <sup>8</sup>R. Schmitt, J. Spring, R. Korobko, and J. L. M. Rupp, "Design of oxygen vacancy configuration for memristive systems," ACS Nano 11, 8881–8891 (2017).
- <sup>9</sup>M. Pianassola, M. Loveday, J. W. McMurray, M. Koschan, C. L. Melcher, and M. Zhuravleva, "Solid-state synthesis of multicomponent equiatomic rare-earth oxides," J. Am. Ceram. Soc. 103, 2908–2918 (2020).
- <sup>10</sup>R. Witte, A. Sarkar, R. Kruk, B. Eggert, R. A. Brand, H. Wende, and H. Hahn, "High-entropy oxides: An emerging prospect for magnetic rare-earth transition metal perovskites," Phys. Rev. Mater. 3, 034406 (2019).
- <sup>11</sup>G. N. Kotsonis, P. B. Meisenheimer, L. Miao, J. Roth, B. Wang, P. Shafer, R. Engel-Herbert, N. Alem, J. T. Heron, C. M. Rost, and J.-P. Maria, "Property and cation valence engineering in entropy-stabilized oxide thin films," Phys. Rev. Mater. 4, 100401 (2020).
- <sup>12</sup>P. B. Meisenheimer, L. D. Williams, S. H. Sung, J. Gim, P. Shafer, G. N. Kotsonis, J.-P. Maria, M. Trassin, R. Hovden, E. Kioupakis, and J. T. Heron, "Magnetic frustration control through tunable stereochemically driven disorder in entropy-stabilized oxides," Phys. Rev. Mater. 3, 104420 (2019).

- <sup>13</sup>P. B. Meisenheimer, T. J. Kratofil, and J. T. Heron, "Giant enhancement of exchange coupling in entropy-stabilized oxide heterostructures," Sci. Rep. 7, 13344 (2017).
- <sup>14</sup>G. N. Kotsonis, C. M. Rost, D. T. Harris, and J.-P. Maria, "Epitaxial entropy-stabilized oxides: Growth of chemically diverse phases via kinetic bombard-ment," MRS Commun. 8, 1371–1377 (2018).
- <sup>15</sup>V. Jacobson, D. Diercks, B. To, A. Zakutayev, and G. Brennecka, "Thin film growth effects on electrical conductivity in entropy stabilized oxides," J. Eur. Ceram. Soc. 41, 2617–2624 (2021).
- <sup>16</sup>M. V. Kante, H. Hahn, S. S. Bhattacharya, and L. Velasco, "Synthesis and characterization of dense, rare-earth based high entropy fluorite thin films," J. Alloys Compd. 947, 169430 (2023).
- <sup>17</sup>G. Adachi and N. Imanaka, "The binary rare earth oxides," Chem. Rev. 98, 1479–1514 (1998).
- <sup>18</sup>M. Coduri, M. Scavini, M. Allieta, M. Brunelli, and C. Ferrero, "Defect structure of Y-doped ceria on different length scales," Chem. Mater. 25, 4278–4289 (2013).
- <sup>19</sup>P. M. Reimer, H. Zabel, C. P. Flynn, and J. A. Dura, "Extraordinary alignment of Nb films with sapphire and the effects of added hydrogen," Phys. Rev. B 45, 11426–11429 (1992).
- <sup>20</sup>E. Schweda and Z. Kang, "Structural features of rare earth oxides," in *Binary Rare Earth Oxides*, edited by G. Adachi, N. Imanaka, and Z. C. Kang (Kluwer Academic Publishers, Dordrecht, 2005), pp. 57–93.
- <sup>21</sup>R. W. G. Wyckoff, *Crystal Structures* (Interscience, 1964).
- <sup>22</sup>G. Brauer and H. Gradinger, "Uber heterotype mischphasen bei seltenerdoxyden. I," Z. Anorg. Allg. Chem. 276, 209–226 (1954).
- 23J. Gjønnes and A. F. Moodie, "Extinction conditions in the dynamic theory of electron diffraction," Acta Cryst. 19, 65–67 (1965).
- <sup>24</sup>H. Asakura, T. Shishido, S. Fuchi, K. Teramura, and T. Tanaka, "Local structure of Pr, Nd, and Sm complex oxides and their x-ray absorption near edge structure spectra," J. Phys. Chem. C 118, 20881–20888 (2014).
- <sup>25</sup>H. Asakura, S. Hosokawa, K. Teramura, and T. Tanaka, "Local structure study of lanthanide elements by x-ray absorption near edge structure spectroscopy," Chem. Rec. 19, 1420–1431 (2019).
- <sup>26</sup>See https://www.jstage.jst.go.jp/article/geochemj/43/3/43\_1.0013/\_article for "Determination of the host phase of rare earth elements in natural carbonate using X-ray absorption near-edge structure" (accessed March 25, 2024).
- <sup>27</sup>T. S. Wu, H. D. Li, Y. W. Chen, S. F. Chen, Y. S. Su, C. H. Chu, C. W. Pao, J. F. Lee, C. H. Lai, H. T. Jeng, S. L. Chang, and Y. L. Soo, "Unconventional interplay between heterovalent dopant elements: Switch-and-modulator band-gap engineering in (Y, Co)-codoped CeO<sub>2</sub> nanocrystals," Sci. Rep. 5, 15415 (2015).
- <sup>28</sup>J. Hormes, M. Pantelouris, G. B. Balazs, and B. Rambadu, "X-ray absorption near edge structure (XANES) measurements of ceria-based solid electrolytes," Solid State Ionics 136-137, 945-954 (2000).
- <sup>29</sup>S. H. Overbury, D. R. Huntley, D. R. Mullins, and G. N. Glavee, "XANES studies of the reduction behavior of (Ce<sub>1-y</sub>Zr<sub>y</sub>)O<sub>2</sub> and Rh/(Ce<sub>1-y</sub>Zr<sub>y</sub>)O<sub>2</sub>," Catal. Lett. 51, 133–138 (1998).
- <sup>30</sup>F. W. Lytle, G. null van der Laan, R. B. Greegor, E. M. Larson, C. E. Violet, and J. Wong, "Determination of the valence of Pr, Gd, and Ho in YBa<sub>2</sub>Cu<sub>3</sub>O<sub>7</sub> by x-ray absorption spectroscopy," Phys. Rev. B 41, 8955–8963 (1990).
- <sup>31</sup>H. A. Harwig, "On the structure of bismuthsesquioxide: The alpha, beta, gamma, and delta-phase," Z. Anorg. Allg. Chem. 444, 151–166 (1978).
- $^{52}$ C. E. Mohn, S. Stølen, S. T. Norberg, and S. Hull, "Oxide-ion disorder within the high temperature  $\delta$  phase of Bi<sub>2</sub>O<sub>3</sub>," Phys. Rev. Lett. **102**, 155502 (2009).